


Cite this: *Dalton Trans.*, 2024, **53**, 8756

## N/P-doped NiFeV oxide nanosheets with oxygen vacancies as an efficient electrocatalyst for the oxygen evolution reaction†

Jingyuan Zhang,<sup>a</sup> Zhen Ma,<sup>a,b</sup> Lanqi Wang,<sup>a</sup> Hui Ni,<sup>a</sup> Jianing Yu<sup>a</sup> and Bin Zhao \*<sup>a</sup>

Plasma treatment as an effective strategy can simultaneously achieve surface modification and heteroatom doping. Here, an N/P-doped NiFeV oxide nanosheet catalyst (N/P-NiFeVO) constructed by Ar/PH<sub>3</sub> plasma treatment is used to drive the oxygen evolution reaction (OER). The introduction of V species leads to the formation of an ultrathin ordered nanostructure and exposure of more active sites. Compared to the 2D NiFeV LDH, the prepared N/P-NiFeVO by plasma treatment possesses multiple-valence Fe, V and Ni species, which regulate the intrinsic electronic structure and enable a superior catalytic activity for the OER in alkaline media. Specifically, the N/P-NiFeVO only require an overpotential of 273 mV to drive the current density of 100 mA cm<sup>-2</sup>. What's more, the electrode can maintain a stable current density in a long-term oxygen evolution reaction (~120 h) under alkaline conditions. This work provides new insight for the rational design of mixed metal oxides for OER electrocatalysts.

Received 31st March 2024,

Accepted 25th April 2024

DOI: 10.1039/d4dt00943f

rsc.li/dalton

### Introduction

Hydrogen is considered to be a clean energy source with high energy density that can solve the problem of depletion of fossil resources and rapid consumption of energy.<sup>1–4</sup> Electrochemical water splitting is considered to be one of the most efficient and sustainable strategies to produce hydrogen.<sup>5,6</sup> Unfortunately, the sluggish kinetics during the OER process seriously affects the energy conversion efficiency.<sup>7,8</sup> Noble metal Ru-based materials with best performance suffer from high cost and poor durability, which hinders development of renewable energy technologies.<sup>9,10</sup> Thus, it is of great importance to develop OER electrocatalysts with low cost and high activity.<sup>11,12</sup>

In the last few decades, a great variety of transition metal-based catalysts with low cost and high activities have been widely investigated, especially layered double hydroxides (LDHs).<sup>13–16</sup> These materials are distinct 2D layer materials with excellent physicochemical characteristics, which makes it appropriate to design various hybrid materials with ion doping to improve the electrochemical activities. However, the OER activity of LDHs is limited by the low number of active

sites at the edges and weak conductivity. Plasma treatment has been considered an efficient strategy to accelerate the OER process.<sup>17–19</sup> It is found that surface etching and heteroatom doping can be achieved simultaneously under certain conditions, which can not only increase the active surface area, but also regulate the energy barrier during the OER process. Wang *et al.* reported a CoFe LDH and Co<sub>3</sub>O<sub>4</sub> nanosheets with oxygen vacancies, which were created using plasma in Ar/water vapour. It is observed that the CoFe LDH and Co<sub>3</sub>O<sub>4</sub> nanosheet catalysts exhibit lower overpotential values, meanwhile the Tafel value is only 68 mV dec<sup>-1</sup>.<sup>20</sup> These results provide strong explanation for the successful improvement of OER performance. Liang *et al.* fabricated NiCoP nanosheets through Ar/PH<sub>3</sub> plasma.<sup>21</sup> The prepared nanosheets showed a lower potential value of 273 mV at a current density of 100 mA cm<sup>-2</sup>.

Herein, a novel approach is designed to fabricate an N/P-decorated Ni-Fe-V oxide electrocatalyst (N/P-NiFeVO). Facile preparation was realized by plasma treatment, which provided a greatly distinctive nanosheet structure, which was obtained from NiFeV-LDH precursors. The obtained NiFeV LDH with plasma treatment shows N/P doping and the formation of oxygen vacancies, which can largely enhance the electrochemical performance by providing a larger electrochemically active surface area and increased active sites. As an OER electrode, N/P-NiFeVO exhibited a low overpotential (273 mV at 100 mA cm<sup>-2</sup>) and an ultra-small Tafel value (34 mV dec<sup>-1</sup>) in 1 M KOH aqueous electrolyte. And it showed a stable catalytic activity with a high current density of 100 mA

<sup>a</sup>School of Materials and Chemistry, University of Shanghai for Science and Technology, Shanghai 200093, China. E-mail: zhaobin@usst.edu.cn

<sup>b</sup>Business development, Edwards Limited, Shanghai, China

† Electronic supplementary information (ESI) available. See DOI: <https://doi.org/10.1039/d4dt00943f>

$\text{cm}^{-2}$  for 120 h. This work sheds light on the preparation of high efficiency electrocatalysts.

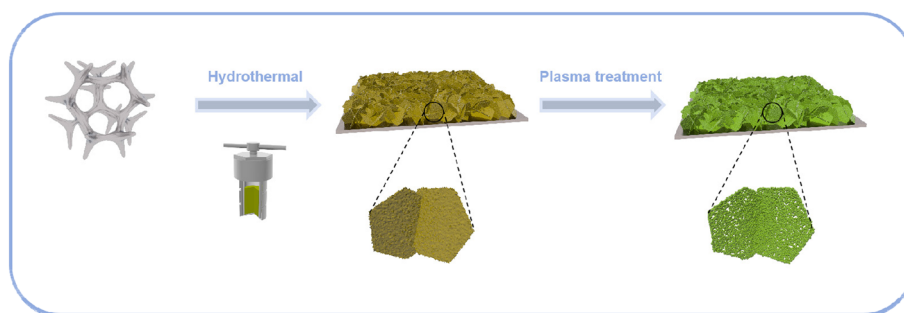
## Results and discussion

Scheme 1 is a schematic diagram of the synthesis procedure of N/P-NiFeVO. A one-step hydrothermal method is first carried out to synthesize a V-doped NiFe LDH on Ni foam (denoted as NiFeV LDH). Then, a nanostructure consisting of N/P-NiFeVO nanosheets with rich O vacancies is constructed *via* the following  $\text{N}_2/\text{PH}_3$  plasma reduction step. As revealed in Fig. S2,<sup>†</sup> an optimum hydrothermal reaction time can result in the best OER performance. The NiFeV LDH-3 h precursor presents a smaller overpotential, lower Tafel slope and optimum charge transfer resistance than the other as-prepared samples. Consequently, the precursor prepared through a hydrothermal reaction of 3 h was chosen as the optimum sample.

X-ray diffraction (XRD) spectroscopy was then employed to investigate the phase structure of the NiFeV LDH precursor and N/P-NiFeVO. The diffraction peaks in Fig. 1a can be well assigned to the NiFe LDH (JCPDS no. 26-1286). After  $\text{N}_2$  plasma treatment, all peaks in Fig. 1b from the NiFeV LDH vanish and the new diffraction peaks can be ascribed to the (111), (220), (311), (222), (400), (422), (511)

and (440) planes of cubic  $\text{NiFe}_2\text{O}_4$  (JCPDS no. 54-0964), demonstrating successful conversion from the LDH to the  $\text{NiFe}_2\text{O}_4$  phase. The peaks appearing at  $36.9^\circ$  can be attributed to the (111) plane of  $\text{VP}_2$  (JCPDS: 30-1426). Additionally, the additional peak appearing at  $40.7^\circ$  can be attributed to the (111) plane of  $\text{Fe}_2\text{P}$  (JCPDS: 51-0943) and  $\text{Ni}_2\text{P}$  (JCPDS: 03-0953).

The initial NiFeV LDH and N/P-NiFeVO nanosheets mentioned above were synthesized and the surface morphology was characterized by scanning electron microscopy (SEM) as shown in Fig. 2a and b and transmission electron microscopy (TEM) as shown in Fig. 2c–g. The N/P-NiFeVO sample shows a similar nanosheet morphology, and plasma etching was employed to introduce more oxygen vacancies into the precursor. The TEM images revealed a relatively rough surface with small irregular pores on the ultrathin nanosheets, relative to the smooth surface of the pristine NiFeV LDH. The high-resolution TEM (HRTEM, Fig. 2d–g) images indicate the lattice fringe spacing of 0.15 nm and 0.25 nm consistent with the (440) and (311) planes characteristic of  $\text{NiFe}_2\text{O}_4$  nanosheets. However, the 0.22 nm and 0.24 nm lattice fringes at the edges are attributed to the (111) and (111) planes of  $\text{Ni}_2\text{P}/\text{Fe}_2\text{P}$  (Fig. 2f and g), implying that the plasma etching preserves the P species. Furthermore, the selected area electron diffraction (SAED) pattern of N/P-NiFeVO can be well indexed to all the planes of  $\text{Ni}_2\text{P}$  and  $\text{Fe}_2\text{P}$  (Fig. 2h). The energy-dispersive X-ray



**Scheme 1** Schematic illustration of the synthesis procedure of N/P-NiFeVO@NF.

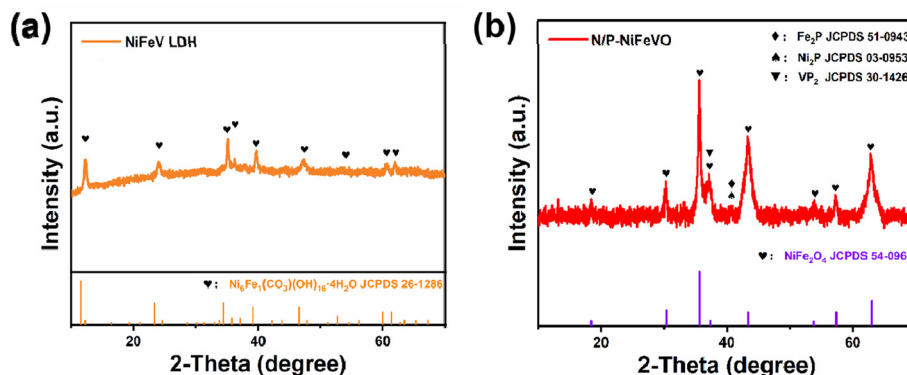


**Fig. 1** XRD patterns of NiFeV-LDH (a) and N/P-NiFeVO (b).

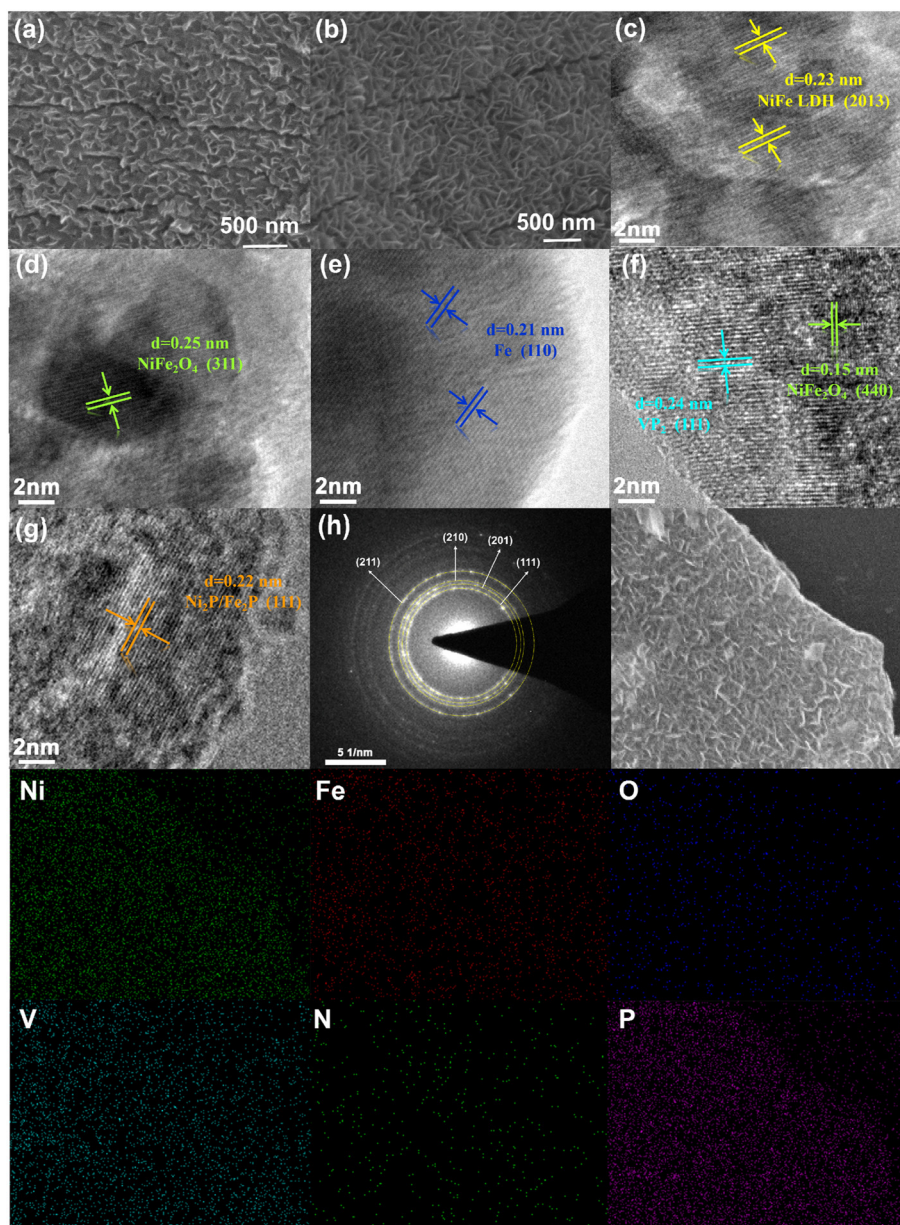


Fig. 2 SEM (a) and HRTEM (c) images of the NiFeV LDH; (b) SEM and HRTEM (d–g) images of N/P-NiFeVO; (h) SAED pattern and the corresponding EDS elemental mapping of N/P-NiFeVO.

spectroscopy (EDX) mapping images of N/P-NiFeVO show an atomic-level distribution of Ni, Fe, V, O, N and P in the whole nanosheet, manifesting the successful fabrication of N/P-NiFeVO.

X-ray photoelectron spectroscopy (XPS) was performed to further investigate the chemical environment and valence states of the NiFeV LDH and N/P-NiFeVO. For the NiFeV LDH, the XPS spectra of Ni 2p can be fitted with two distinct doublets ( $2p_{3/2}$  and  $2p_{1/2}$ ). The peaks at 852.3 and 869.2 eV can be ascribed to the metal Ni, while the peaks at about 855.6 and 873.7 eV correspond to  $\text{Ni}^{2+}$ .<sup>22,23</sup> Regarding N/P-NiFeVO, the characteristic peaks at 856 and

870.3 eV in the Ni 2p spectrum indicate the presence of  $\text{Ni}^{+}$ ,<sup>24</sup> as shown in Fig. 3a. In addition, after plasma treatment, the appearance of  $\text{Fe}^{2+}$  and  $\text{Fe}^0$  peaks confirms the partial reduction of the sample by  $\text{PH}_3$  plasma<sup>25</sup> (Fig. 3b). In Fig. 3c, in comparison with the NiFeV LDH, the binding energy of V 2p of N/P-NiFeVO shifts to a lower binding energy, and the content of  $\text{V}^{3+}$  notably increases, which results from the reduction effect of  $\text{PH}_3$  plasma.<sup>26</sup> In Fig. 3d, the peaks at 529.8, 531.3 and 532.4 eV are assigned to the M–O, oxygen vacancies and oxygen of adsorbed water, respectively.<sup>27</sup> The intensities of oxygen vacancies and M–O of N/P-NiFeVO are enhanced compared to those of the NiFe

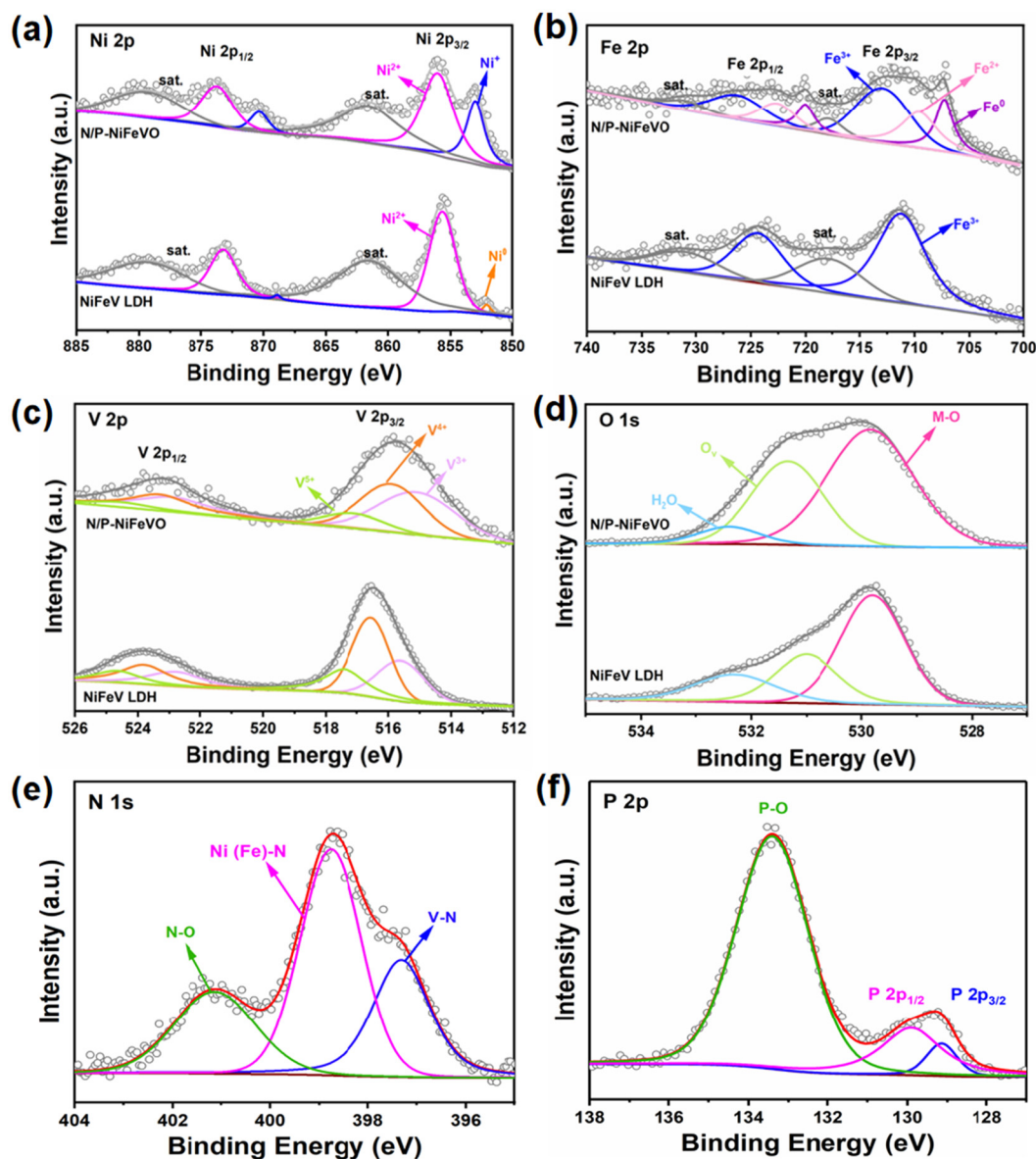
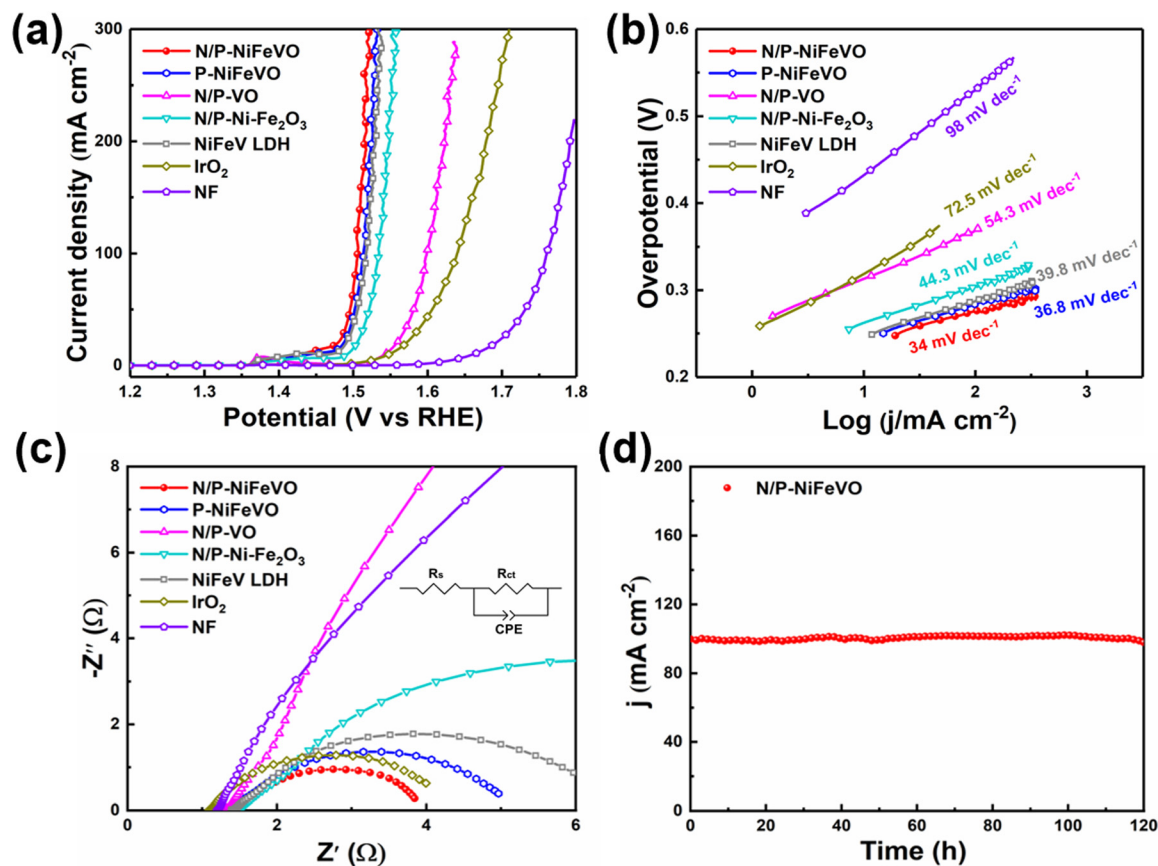


Fig. 3 High-resolution XPS spectra of N/P-NiFeVO and NiFeV LDH: (a) Ni 2p, (b) Fe 2p, (c) V 2p, (d) O 1s, (e) N 1s and (f) P 2p.

LDH, indicating that the plasma etching employed introduced more oxygen vacancies into N/P-NiFeVO. The spectra of N 1s in Fig. 3e reveal the information about the valence states and chemical compositions. The N 1s spectra can be fitted with three peaks at 397.3, 398.8 and 401.1 eV, which are ascribed to V-N, Ni (Fe)-N, and N-O, respectively.<sup>28,29</sup> In the P 2p spectrum (Fig. 3f), the peaks at 129.1 and 129.9 eV correspond to P 2p<sub>3/2</sub> and P 2p<sub>1/2</sub> of metal phosphide, and the peak at 133.4 eV is associated with P-O.<sup>30</sup>

Subsequently, the OER performances of N/P-NiFeVO and derived samples were evaluated in 1 M KOH aqueous electrolyte using a standard three-electrode configuration (Fig. 4a). All potentials were iR-compensated and converted to a reversible hydrogen electrode (RHE) scale. As expected, compared

with P-NiFeVO, N/P-VO, N/P-Ni Fe<sub>2</sub>O<sub>3</sub>, NiFeV LDH and IrO<sub>2</sub>, N/P-NiFeVO exhibited the lowest overpotential at the same current density (273 mV at 100 mA cm<sup>-2</sup>) and an ultra-small Tafel value (34 mV dec<sup>-1</sup>), suggesting that the plasma etched electrocatalyst with ultrathin nanosheets can serve as a good electrocatalytically active species for the OER (Fig. 4b). Noteworthy, such a low overpotential is superior to those of many OER heterostructured catalysts (Table S1†). In addition, the electrochemically active area (ECSA) was calculated from cyclic voltammetry (Fig. 5) at different scan rates from 20 to 120 mV s<sup>-1</sup> within the non-faradaic potential range. It is clear that the ECSA of N/P-NiFeVO nanosheets with plasma treatment is larger than that of the NiFeV LDH material. In other words, the surface reconstruction by plasma treatment does



**Fig. 4** OER electrocatalytic performance of various electrodes in 1 M KOH. (a) LSV curves (with iR correction) at a scan rate of  $2 \text{ mV s}^{-1}$ ; (b) Tafel slopes; (c) Nyquist plots; inset: the equivalent circuit used for data analyses. (d) The chronoamperometric curve of N/P-NiFeVO at a constant current density of  $100 \text{ mA cm}^{-2}$  over 120 h.

not compromise the high specific surface of the original catalyst. As shown in Fig. 5f, the  $C_{dl}$  of N/P-NiFeVO is  $3 \text{ mF cm}^{-2}$ , noticeably larger than that of the NiFeV LDH and its derivatives ( $1.5 \text{ mF cm}^{-2}$ ), which indicates that more active sites were generated. To gain more insights into the intrinsic activity for the OER, the LSV polarization curves were normalized with ECSA. As depicted in Fig. S4,† N/P-NiFeVO possesses superior intrinsic catalytic activity compared to the other catalysts.<sup>31,32</sup> It can be inferred that N/P-NiFeVO constructed by plasma treatment has more exposed active sites, which enable its remarkable catalytic activities.<sup>33,34</sup>

At the same time, its stability is also outstanding, showing good stability up to 120 h with little change at a constant current density of  $100 \text{ mA cm}^{-2}$  (Fig. 4d). Further SEM images of the post-OER catalyst show a rougher structure with irregular clusters on nanosheets (Fig. S5†). In the surface oxidation under anodic voltage, the morphology of the catalyst was largely retained compared to that of the as-prepared sample. After the OER test, the high-resolution XPS spectra of Ni 2p (Fig. S6a†) show two peaks ascribed to  $\text{Ni}^{2+}$ , while the  $\text{Ni}^0$  peak completely disappeared. In addition, the only remaining  $\text{Fe}^{3+}$  peak confirms the com-

plete oxidation of  $\text{Fe}^0$  and  $\text{Fe}^{2+}$  (Fig. S6b†). In Fig. S6c,† the peaks at 530.3, 531.3 and 532.6 eV are assigned to the M–O, oxygen vacancies and oxygen of adsorbed water, respectively.<sup>35,36</sup> Fig. S6d† shows peaks at 515.4, 516.2 and 517.1 eV, which are assigned to  $\text{V}^{3+}$ ,  $\text{V}^{4+}$  and  $\text{V}^{5+}$ . Compared to those of N/P-NiFeVO, the intensities of V–N, Ni (Fe)–N and N–O of the post-OER catalyst weakened and the P 2p peak completely disappeared, which is due to the intense oxidation process (Fig. S6e and f†).

To evaluate the durability of N/P-NiFeVO in alkaline media, we assembled a two-electrode system simulating a water splitting cell using Pt/C as a hydrogen evolution catalyst and N/P-NiFeVO as an oxygen evolution catalyst. As shown in Fig. 6a, the cell voltages in alkaline media of Pt/C||N/P-NiFeVO and Pt/C|| $\text{IrO}_2$  are  $1.56 \text{ V}@10 \text{ mA cm}^{-2}$  and  $1.62 \text{ V}@10 \text{ mA cm}^{-2}$ , respectively. Moreover, for the Pt/C||N/P-NiFeVO, the cell voltage can remain at a similar level even after continuous working for 120 h. Such a performance for water electrolysis is better than that of most recently reported NiFe-based electrocatalysts (Table S2†). Overall, these results clearly indicate that N/P-NiFeVO is indeed a competent and persistent OER catalyst.

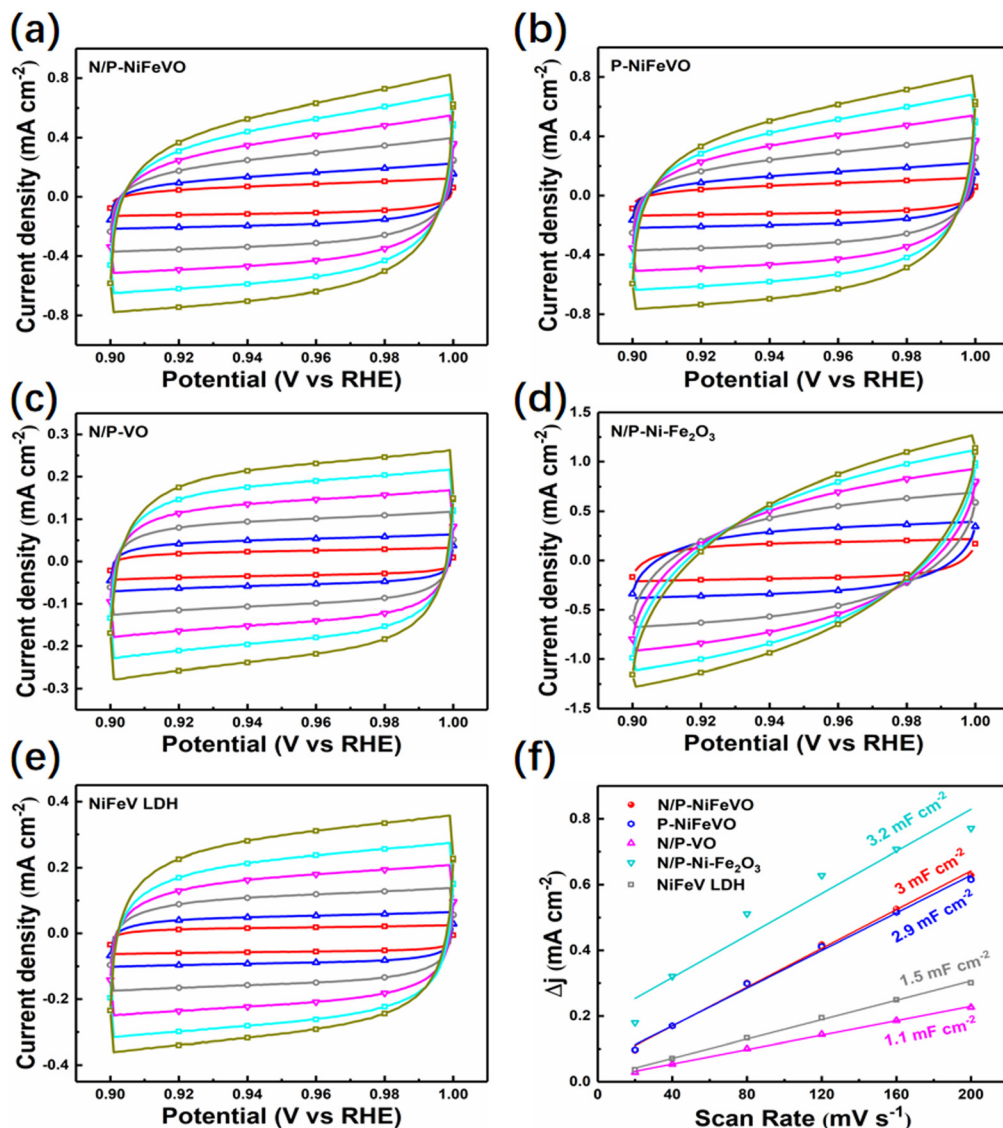


Fig. 5 Cyclic voltammograms at different scan rates (20–200 mV s<sup>-1</sup>) in the potential range of 0.9–1.0 V vs. RHE for the various electrocatalysts: (a) N/P-NiFeVO, (b) P-NiFeVO, (c) N/P-VO, (d) N/P-Ni-Fe<sub>2</sub>O<sub>3</sub>, and (e) NiFeV LDH. (f) Difference in current density plotted against the scan rate for various samples showing the extraction of the double-layer capacitances.

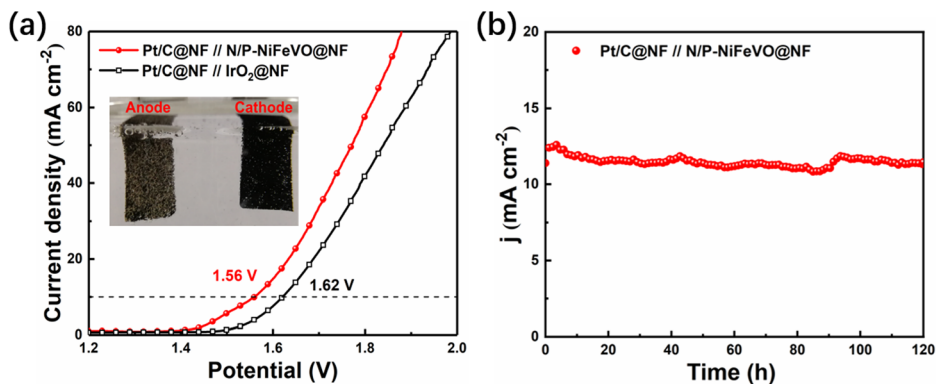


Fig. 6 (a) Polarization curves (without iR correction) of Pt/C@NF//N/P-NiFeVO@NF and Pt/C@NF//IrO<sub>2</sub>@NF at a scan rate of 2 mV s<sup>-1</sup> for overall water splitting; the inset shows the photograph of the electrolyzer powered by a battery of 1.56 V. (b) The chronoamperometric curve of the Pt/C@NF//N/P-NiFeVO@NF cell at a constant current density of 10 mA cm<sup>-2</sup> over 120 h.

## Conclusion

In summary, a well-aligned N/P-doped NiFeVO oxide nanosheet catalyst was prepared by Ar/PH<sub>3</sub> plasma treatment of the NiFe LDH. Plasma treatment not only leads to the transformation of the NiFe LDH to NiFeVO nanosheets, but also induces the formation of oxygen vacancies. Accordingly, the N/P-doped NiFeVO nanosheets with a high specific surface area and plentiful pores provide unobstructed channels for electrolyte ion diffusion and boosted charge transfer kinetics. These advantages endow the N/P-doped NiFeVO electrode with outstanding electrochemical properties. This work shows that tuning the synthesis conditions and composition of mixed metal oxides is an effective strategy to enhance the catalytic performance for the OER.

## Conflicts of interest

The authors declare that they have no known competing financial interests or personal relationships that could have appeared to influence the work reported in this paper.

## Acknowledgements

Financial support from the Natural Science Foundation of Shanghai (21ZR1445700) and the Science and Technology Commission of Shanghai Municipality (23440790400) is gratefully acknowledged.

## References

- L. Xu, S. Wu, X. He, H. Wang, D. Deng, J. Wu and H. Li, *Chem. Eng. J.*, 2022, **437**, 135291.
- P. Erickson, M. Lazarus and G. Piggot, *Nat. Clim. Change*, 2018, **8**, 1037–1043.
- F. P. Perera, *Environ. Health Perspect.*, 2017, **125**, 141–148.
- R. Gao and D. P. Yan, *Adv. Energy Mater.*, 2020, **10**, 1900954.
- T. R. Cook, D. K. Dogutan, S. Y. Reece, Y. Surendranath, T. S. Teets and D. G. Nocera, *Chem. Rev.*, 2010, **110**, 6474–6502.
- R. Gao, H. Zhang and D. P. Yan, *Nano Energy*, 2017, **31**, 90–95.
- N. T. Suen, S. F. Hung, Q. Quan, N. Zhang, Y. J. Xu and H. M. Chen, *Chem. Soc. Rev.*, 2017, **46**, 337–365.
- M. Arif, G. Yasin, M. Shakeel, M. A. Mushtaq, W. Ye, X. Y. Fang, S. F. Ji and D. P. Yan, *Mater. Chem. Front.*, 2019, **3**, 520–531.
- D. Chen, R. Lu, Z. Pu, J. Zhu, H. W. Li, F. Liu, S. Hu, X. Luo, J. Wu, Y. Zhao and S. Mu, *Appl. Catal., B*, 2020, **279**, 119396.
- Y. Lee, J. Suntivich, K. J. May, E. E. Perry and Y. Shao-Horn, *J. Phys. Chem. Lett.*, 2012, **3**, 399–404.
- Q. Q. Ji, Y. Kong, H. Tan, H. L. Duan, N. Li, B. Tang, Y. Wang, S. H. Feng, L. Y. Lv, C. Wang, F. C. Hu, W. H. Zhang, L. Cai and W. S. Yan, *ACS Catal.*, 2022, **12**, 4318–4326.
- S. Jin, *ACS Energy Lett.*, 2017, **2**, 1937.
- G. F. Chen, T. Y. Ma, Z. Q. Liu, N. Li, Y. Z. Su, K. Davey and S. Z. Qiao, *Adv. Funct. Mater.*, 2016, **26**, 3314–3323.
- J. Yu, T. A. Le, N. Q. Tran and H. Lee, *Chem. – Eur. J.*, 2020, **26**, 6423–6436.
- C. Hu, L. Zhang and J. Gong, *Energy Environ. Sci.*, 2019, **12**, 2620–2645.
- S. Dresp, F. Dionigi, M. Klingenhof, T. Merzdorf, H. Schmies, J. Drnec, A. Poulain and P. Strasser, *ACS Catal.*, 2021, **11**, 6800–6809.
- F. Song and X. Hu, Exfoliation of layered double hydroxides for enhanced oxygen evolution catalysis, *Nat. Commun.*, 2014, **5**, 4477.
- L. Ma, I. Jia, X. Guo and L. Xiang, *Chin. J. Catal.*, 2014, **35**, 108–119.
- A. U. Haq, S. Askari, A. McLister, S. Rawlinson, J. Davis, S. Chakrabarti, V. Svrcek, P. Maguire, P. Papakonstantinou and D. Mariotti, *Nat. Commun.*, 2019, **10**, 1–8.
- R. Liu, Y. Wang, D. Liu, Y. Zou and S. Wang, *Adv. Mater.*, 2017, **29**, 1–7.
- H. Liang, A. N. Gandi, D. H. Anjum, X. Wang, U. Schwingenschlögl and H. N. Alshareef, *Nano Lett.*, 2016, **16**, 7718–7725.
- A. L. Wang, H. Xu and G. R. Li, *ACS Energy Lett.*, 2016, **1**, 445–453.
- H. J. Zhang, X. P. Li, A. Hähnel, V. Naumann, C. Lin, S. Azimi, S. L. Schweizer, A. W. Maijenburg and R. B. Wehrspohn, *Adv. Funct. Mater.*, 2018, **28**, 1706847.
- P. Zhou, D. N. Xing, Y. Y. Liu, Z. Y. Wang, P. Wang, Z. K. Zheng, X. Y. Qin, X. Y. Zhang, Y. Dai and B. B. Huang, *J. Mater. Chem. A*, 2019, **7**, 5513–5521.
- X. L. Liu, X. S. Lv, P. Wang, Q. Q. Zhang, B. B. Huang, Z. Y. Wang, Y. Y. Liu, Z. K. Zheng and Y. Dai, *Electrochim. Acta*, 2020, **333**, 135488.
- Y. M. Hu, Z. L. Wang, W. J. Liu, L. Xu, M. L. Guan, Y. P. Huang, Y. Zhao, J. Bao and H. M. Li, *ACS Sustainable Chem. Eng.*, 2019, **7**, 16828–16834.
- H. H. Lv, X. B. Zhang, F. M. Wang, G. J. Lv, T. T. Yu, M. L. Lv, J. W. Wang, Y. Zhai and J. Q. Hu, *J. Mater. Chem. A*, 2020, **8**, 14287–14298.
- M. L. Yan, K. Mao, P. X. Cui, C. Chen, J. Zhao, X. Z. Wang, L. J. Yang, H. Yang, Q. Wu and Z. Hu, *Nano Res.*, 2020, **13**, 328–334.
- S. S. Tan, Y. H. Dai, Y. L. Jiang, Q. L. Wei, G. B. Zhang, F. Y. Xiong, X. Q. Zhu, Z. Y. Hu, L. Zhou, Y. C. Jin, K. Kanamura, Q. Y. An and L. Q. Mai, *Adv. Funct. Mater.*, 2020, 2008034.
- M. J. Guo, S. Y. Song, S. S. Zhang, Y. Yan, K. Zhan, J. H. Yang and B. Zhao, *ACS Sustainable Chem. Eng.*, 2020, **8**, 7436–7444.
- N. Li, L. Cai, C. Wang, Y. Lin, J. Z. Huang, H. Y. Sheng, H. B. Pan, W. Zhang, Q. Q. Ji, H. L. Duan, W. Hu, W. H. Zhang, F. C. Hu, H. Tan, Z. H. Sun, B. Song, S. Jin and W. S. Yan, *J. Am. Chem. Soc.*, 2021, **143**, 18001–18009.

- 32 N. Li, L. Cai, G. P. Gao, Y. Lin, C. Wang, H. J. Liu, Y. Y. Liu, H. L. Duan, Q. Q. Ji, W. Hu, H. Tan, Z. M. Qi, L. W. Wang and W. S. Yan, *Nano Lett.*, 2022, **22**, 6988–6996.
- 33 Y. Yan, C. Liu, H. Jian, X. Cheng, T. Hu, D. Wang, L. Shang, G. Chen, P. Schaaf, X. Wang, E. Kan and T. Zhang, *Adv. Funct. Mater.*, 2021, **31**, 2009610.
- 34 Z. Wang, B. Xiao, Z. Lin, Y. Xu, Y. Lin, F. Meng, Q. Zhang, L. Gu, B. Fang, S. Guo and W. Zhong, *Angew. Chem., Int. Ed.*, 2021, **60**, 23388–23393.
- 35 Z. Xu, Y. Ying, G. Zhang, K. Li, Y. Liu, N. Fu, X. Guo, F. Yu and H. Huang, *J. Mater. Chem. A*, 2020, **8**, 26130.
- 36 S. Klaus, Y. Cai, M. W. Louie, L. Trotochaud and A. T. Bell, *J. Phys. Chem. C*, 2015, **119**, 7243.